

Tracing the Galactic Disk with Planetary Nebulae using Gaia DR3

Distance Catalog, Velocities, Populations, and Radial Metallicity Gradients of Galactic Planetary Nebulae

B. Bucciarelli¹ and L. Stanghellini²

¹ INAF-OATo, Via Osservatorio 20, 10023 Pino Torinese TO, Italy
e-mail: beatrice.bucciarelli@inaf.it

² NSF's NOIRLab, 950 N. Cherry Avenue, Tucson, Arizona 85719, United States
e-mail: letizia.stanghellini@noirlab.edu

Received; Accepted

ABSTRACT

Aims. We want to study the population of Galactic planetary nebulae (PNe) and their central stars (CSs) through the analysis of their distances and Galactic distribution. The PN distances are obtained by means of a revised statistical distance scale, based on an astrometrically-defined sample of CSs from Gaia DR3 as calibrators. The new statistical distances, together with the proper motion of the CSs – also from DR3, and with published PN abundances as well as radial velocities, are used to characterize the PN populations in the Galaxy, and to derive the radial metallicity gradient.

Methods. The statistical scale is applied to infer distances of a significant number (~ 850) of Galactic PNe, for which we deliver a new catalog of PN distances. By adopting a circular velocity curve of the Galaxy, we also obtain peculiar 3D velocities for a large sample of PNe (~ 300). Elemental abundances of the PNe are culled from the literature for an updated catalog, to be used in our analysis and other external applications.

Results. The radial chemical gradient of the Galactic Disk is traced by PNe with available chemical abundances and distances, and kinematic data of the CSs are employed to identify the Halo PN population. We date PN progenitors based both on abundances and on kinematic properties, finding a confirmation of the first method with the second. For all PNe with at least one oxygen determination in the literature, we find a slope of the radial oxygen gradient equal to $\Delta \log(\text{O}/\text{H})/\Delta R_G = -0.0144 \pm 0.00385$ [dex kpc⁻¹]. Furthermore, we estimate radial oxygen gradients for the PNe with old (> 7.5 Gyr) and young (< 1 Gyr) progenitors to be respectively $\Delta \log(\text{O}/\text{H})/\Delta R_G = -0.0121 \pm 0.00465$ and -0.022 ± 0.00758 [dex kpc⁻¹], thus disclosing a mild steepening of the gradient since Galaxy formation, with a slope change of 0.01 dex. The time evolution is slightly higher (~ 0.015 dex) if we select the best available abundances in the literature. This result is in broad agreement with previous PN results, but now based on DR3 Gaia analysis, and also in agreement with what traced by most other Galactic probes. We also find a moderate oxygen enrichment when comparing the PNe with young and old progenitors.

Key words. (ISM): Planetary Nebulae – Galaxy: disk – Galaxy: evolution – stars: distances – methods: statistical

1. Introduction

The third data release of the Gaia ESA mission, DR3 (Gaia Collaboration et al. 2016, 2023b) provides unprecedented astrometric – along with photometric and spectroscopic – data for hundreds of central stars (CSs) of planetary nebulae (PNe) that, further to witnessing a short-lived phase of their life, turn out to be suitable probes of chemical abundances in the Galaxy (e.g. Peimbert 1978; Henry et al. 2010), as well as in external galaxies (see Stanghellini 2019, and references therein). Metal contents of PNe with young and old progenitors can be examined to constrain different mechanisms of gas accretion and star formation history (e.g. Gibson et al. 2013; Curti et al. 2020).

In particular, metallicity gradients along galactic discs are crucial observables in galaxy evolution studies. They are the outcome of complex interacting physical processes involving metal production, consumption, transport, and loss (Matteucci 2021; Prantzos et al. 2023); currently, their radial profiles reconstructed from different metal tracers show some diversities which need to be further investigated (Stanghellini et al. 2019). The basic observational step in this direction is to build a metallicity gradient

as function of the galactocentric radius R_G ; the profile and slope of the gradient can be inspected for a coeval stellar population, and its time evolution tested with different age populations (e.g. Magrini et al. 2016; Stanghellini & Haywood 2018). To this end, being able to gauge the precise PN location as function of Galactic radius is clearly of utmost importance.

In our previous paper (Stanghellini et al. 2020, hereafter Paper I), we performed a re-calibration of the PN statistical distance scale from a sample of ≈ 100 CSs having DR2 parallaxes with relative uncertainty better than 20%, demonstrating the potential of Gaia astrometry in improving the extant knowledge on PNe distances. Following on this path, we present a revision of the PN distance scale using the best parallaxes available from Gaia DR3 (Lindgren et al. 2021b). In addition, the highly accurate Gaia DR3 proper motions are precious parameters in the context of this study: in fact, space velocities can be inferred by the CS proper motions using their distances. Since the velocity dispersion of a disk population tends to increase with stellar age (e.g. Strömberg 1925, 1946; Wielen 1977; Mackereth et al. 2019), the kinematic properties of PNe CSs bear independent

information about the progenitor's age, which can complement and support the elemental abundance dating method. Therefore, in this work we have exploited the full astrometric data provided by Gaia DR3 for a bona-fide set of Galactic PNe, in combination with their most updated chemical abundances and radial velocities, to investigate the gas-phase metallicity gradient of the Milky Way and its evolution in time.

The structure of the paper is as follows. In § 2 we characterize the Galactic PN sample and give an assessment of the new distance scale calibration, based on their DR3 parallax and other nebular parameters; § 3 describes the data and methods for the derivation of radial metallicity gradients; finally, § 4 is devoted to the discussion of the results and the conclusions.

2. The Revised Distance Scale

We explore the statistical distance scale for Galactic Planetary Nebulae (PNe) hinging on the commensurate relation between their surface brightness and physical radius advocated by Shklovsky (1956), which has been widely used and refined since then; see Smith (2015) for a thorough review. The similarity between the expansion radius of a fully ionized nebula and the decreasing density of its (nearly) constant ionized mass provides an estimation of the PN distance, once its angular radius and observed flux have been measured.

Despite the wide range of PNe mass progenitors, the so-called Shklovsky mass, i.e., the one responsible for the observed flux, has a fairly constant value of $\approx 0.1 - 0.2 M_{\odot}$, making the underlying assumption that all nebulae have the same ionized mass a viable one. Nonetheless, the Shklovsky method tends to overestimate the distances of less evolved PNe that are in a "ionization bound" state, i.e., whose ionization front is still within the nebular material, far from the edge of the gaseous cloud (Schneider & Buckley 1996).

The wealth and unprecedented accuracy of Gaia DR3 parallaxes allow us to calibrate the *physical radius-surface brightness* distance scale on well-constrained empirical evidence, while allowing us to put to test some of the crucial aspects of the underlying physical models. In logarithmic units, the scale is represented by the equation:

$$\log R = a \times \log S_{H\beta} + b, \quad (1)$$

where the surface brightness $S_{H\beta}$ is the distance-independent parameter, given in terms of the extinction-corrected absolute $H\beta$ flux from the nebula $I_{H\beta}$ (in $\text{erg cm}^{-2} \text{sec}^{-1}$) and its angular radius θ (in arcsec) as $S_{H\beta} = I_{H\beta}/\pi\theta^2$, whereas the physical radius of the PN, $R = \theta''/(206265 p'')$ (in pc), with p the PN's parallax, is the distance-dependent variable.

2.1. Identifying Central Stars of Planetary Nebulae in Gaia DR3

Starting from a list of 2556 *true* PNe extracted from the HASH database (Parker et al. 2016)¹, we searched for Gaia DR3 sources with the HASH coordinates of the nebular centers, inside a radius of 3 arcsec and up to 5 arcsec if the smaller radius returned zero matches. We resolved multiple matches by applying a ranking system based on the astrometric quality indicators provided with the Gaia solution. In such a way, we identified 1674 CS candidates lying near the geometric center of the nebula with a DR3 parallax.

¹ The list includes all objects from the HASH database that were labeled as 'TRUE PN' at the time of this work

Furthermore, to check the reliability of our purely astrometric criterion, we made comparisons with the CS catalogs recently published by González-Santamaría et al. (2021) and Chornay & Walton (2021) whose matching algorithms used the Gaia BP-RP colour to discriminate between hot and cool stars candidates and weigh them accordingly. Since our main aim in this context was sample purity as opposed to completeness, we retained only those objects for which our matched Gaia source was in agreement with both González-Santamaría et al. (2021) and Chornay & Walton (2021) catalogs, obtaining a sample of 942 CSs, whose corresponding PNe constitute our *Calibrator Sample*.

2.2. Selection of Distance Scale Calibrators

To find the parameters a and b of Eq. 1 we matched the Calibrator Sample with the physical parameters that are needed to build the scale. Table 1 contains the Calibrator Sample PNe whose angular radius, $H\beta$ flux, and extinction correction are available in the literature. For each of those targets we list the PN G name, the Gaia DR3 ID name – which is different from the DR2 ID, the common name used for the PN, the corrected (see below) DR3 parallax ϖ_c , the angular radius θ , the logarithmic $H\beta$ flux, the logarithmic extinction constant, and the ionized mass $\log M_i$, the latter calculated following the prescription described in Paper I. For the cases where uncertainties on the physical parameters are unavailable we assume a typical error for each parameter. In particular, we adopt 0.2 as a relative angular radius uncertainty, and 0.1 as the uncertainty for the logarithmic extinction.

All parameters, excluding those derived from Gaia DR3, have been selected from the literature (references in Stanghellini & Haywood 2018). Parallaxes in Table 1 are those used to fit the scale, and have been corrected by applying to DR3 parallaxes a global offset of 0.017 mas plus an additional bias term which depends on the star's G magnitude, its colour $G_{BP} - G_{RP}$ — or *pseudo-colour* in case of a 6-parameter (6p) astrometric solution — and ecliptic latitude, detailed in Lindegren et al. (2021a). Moreover, parallax errors have been multiplied by 1.05/1.22 for a 5p/6p parameter solution to compensate an underestimation (bias) of the error as described in Fabricius et al. (2021). In the following, the symbols ϖ_c , σ_{ϖ_c} will indicate that the corresponding DR3 parallax ϖ and standard error σ_{ϖ} have been corrected for the above mentioned systematic effects.

When we match our Calibrator Sample with the PNe whose radius, $H\beta$ flux, and extinction are also available, we obtain 401 calibrators. If we chose $\sigma_{\varpi_c}/\varpi_c < 20\%$ (10%) we still have 137 (74) calibrators, doubling the corresponding samples in the DR2 calibration (Paper I).

2.3. Building the Planetary Nebula Distance Scale

The semi-empirical relation expressed by Eq. 1 sets the stage for the inference problem relating the sought-for posterior density distribution of the unknown parameters a and b to the likelihood of the observed physical quantities characterizing our PN calibrators. We give here a short exposition of the method, referring the reader to the Appendix of Paper I for a complete derivation.

To formulate our likelihood function, we first introduce the measured radius $\theta \sim N(\phi, \sigma_{\theta})$, flux $I \sim N(J, \sigma_I)$, and parallax $\varpi \sim N(p, \sigma_{\varpi})$ as Gaussian-distributed uncorrelated variables, then marginalize the likelihood of the i -th set of measurements with respect to the parameters radius (ϕ), flux (J), and parallax (p) and treat the parallax as dependent variable through Eq. 1, obtaining the expression of the likelihood for the i -th calibrator

Table 1. PN Calibrators Parameters

PN G	Gaia ID (DR3)	alias	ϖ_c [""]	θ [""]	$F_{H\beta}$ [erg cm ⁻² s ⁻¹]	c	$\log M_i$
000.1+17.2	4130784921205604736	PC12	0.108±0.081	1.1245	-11.91±0.00	0.700±0.10	-1.198
000.1-05.6	4049045783774253696	H2-40	0.361±0.326	8.7950	-13.20±0.40	0.731±0.15	-1.761
000.3+12.2	4126115570219432448	IC4634	0.414±0.052	5.8150	-10.88 ±0.01	0.550±0.06	-1.175

Notes. See main text for a detailed column description.

(The full table is available electronically at the CDS.)

as:

$$L(\varpi_i, \theta_i, I_i | a, b) = \int_0^{\phi_{lim}} \int_0^{J_{lim}} N\left(\frac{\pi^a \phi_i^{2a+1}}{206265 J_i^a 10^b}, \sigma_{\varpi_i}\right) \times N(\phi_i, \sigma_{\theta_i}) N(J_i, \sigma_{I_i}) d\phi dJ, \quad (2)$$

where we have used uniform priors for ϕ and J inside some reasonable intervals. Then, after forming the *log-likelihood* of the complete set of calibrators, by virtue of the Bayes theorem we derive the bi-variate posterior probability density (p_{pdf}) of a and b , assigning them uniform priors, as:

$$p_{pdf}(a, b | \varpi, \theta, I) \propto \sum_{i=1}^N \log \left(\int_0^{\phi_{lim}} \int_0^{J_{lim}} \left(N\left(\frac{\pi^a \phi_i^{2a+1}}{206265 J_i^a 10^b}, \sigma_{\varpi_i}\right) \times N(\phi_i, \sigma_{\theta_i}) N(J_i, \sigma_{I_i}) d\phi dJ \right) \right). \quad (3)$$

We approach this problem by numerical integration over the ϕ and J parameters' range, and by sampling the posterior distribution of a and b inside a bi-dimensional grid with step sizes of 0.0005 and 0.005 for the *slope* and *intercept* parameters, respectively. The estimated \hat{a} and \hat{b} correspond to the mode of the discrete posterior probability density function. The 68% confidence interval for the two parameters are calculated separately, by projecting onto the a and b axes the iso-probability contour of the posterior distribution for which $|p(a, b)_{max} - p(a, b)| \leq 0.5$ (remembering that the log-likelihood ratio statistics is asymptotically distributed as $\chi^2/2$). And finally, we estimate the correlation term from the complete posterior sample, as $\rho_{\hat{a}\hat{b}} = 1/(\sigma_{\hat{a}}\sigma_{\hat{b}}) \sum_{i=1}^{n_a} \sum_{j=1}^{n_b} [p(a_i, b_j)((a_i - \hat{a})(b_j - \hat{b}))]$, obtaining in all cases a high positive correlation between the estimated slope and intercept, as illustrated in Fig. 3 showing density levels of the bi-variate posterior distribution $p_{pdf}(a, b)$ for the $\sigma_{\varpi_c}/\varpi_c < 20\%$ sample.

We inferred the distance scale parameters using different sets of calibrators, defined by the adopted threshold on the relative DR3 parallax error $\sigma_{\varpi_c}/\varpi_c$, obtaining consistent estimations of the scale slope a and intercept b as reported in Table 2. Figure 1 shows the $\log R - \log S_{H\beta}$ plane with the subsets of calibrators for which $\sigma_{\varpi}/\varpi \leq 10\%$ (top panel) and $\sigma_{\varpi_c}/\varpi_c \leq 20\%$ (bottom panel) along with their error bars, and the corresponding estimated linear relation (see caption).

By inspecting these plots, both data sets show a somewhat large dispersion around the scale. Moreover, from a comparison of the 20% sample of Figure 1 with that of Fig. 2 in Paper I (where the calibration used DR2 parallaxes) we note that the numerous "stragglers" populating the lower right end of the plane, which corresponded to PN with very low ionized mass ($\log M_i < -2$), are not so prominent in the new plots.

It turned out that, among the complete set of potential calibrators, 37 objects had $\log M_i < -2$ but none of them had accurate enough parallaxes at the 10% level and a few – indicated in red in the lower panel of Figure 1 – met the 20% requirement. If we put these 37 objects on the $\log R - \log S_{H\beta}$ plane, they are scattered mainly in the lower part of the graph and their distance do not conform with the statistical scale, corroborating the findings of our previous paper based on DR2 data.

To further investigate the ionized mass effect, we inspect the PNe with $\sigma_{\varpi_c}/\varpi_c < 20\%$ by plotting them using a colour-density scale that increases with $\log M_i$. The result, shown in Figure 2, is quite striking and can be fully appreciated thanks to the quality of the calibrators: the dispersion around the linear scale is clearly linked to the (estimated) $\log M_i$ of the PN shell, manifesting the deviation of its actual evolutionary state. In fact, in the transition from ionization-bound, or optically thick, to density-bound, or optically thin, the ionized mass of PNe increases, as discussed in Pottasch (1980); therefore, the model assumption of fully ionized, constant mass on which Eq. 1 stands, does not strictly hold.

Remarkably, when we tried to tighten even more the constraint on the goodness of the parallax relative error we obtained a similar dispersion of the calibrators as in Fig. 2. Finally, by subtracting out the effect due to the nominal uncertainties of the observed angular radius and flux, we tentatively estimated an average intrinsic (cosmic) scatter of ~ 0.1 dex around the distance scale and conclude that this is due to an actual observed nebular evolution which limits the potential accuracy of this statistical distance scale, unless the ionized mass for the PN is known a priori.

The results of the calibration are reported in Table 2, where for each of the three relative uncertainty thresholds on $\sigma_{\varpi_c}/\varpi_c$ we give the number of calibrators N_{cal} , the estimated slope and intercept along with their correlation ρ_{ab} ; we also list the averaged parameter $\langle K \rangle = \langle \text{statistical_scale_distance} \times \varpi_c \rangle$, ideally equal to 1, and its dispersion $\langle \sigma_K \rangle$, which is an indicator of the goodness of the scale, see (Smith 2015).

In this paper we will use the third scale listed in Table 2, the one calibrated with central stars whose DR3 parallaxes were measured with better uncertainty than 20%, which has a $\langle K \rangle \sim 0.964$. Through the analysis presented in this paper we have confirmed that using another of the three scales would not have an impact of the science results. Our adopted scale is:

$$\log R_{PN} = (-0.242 \pm 0.0042) \times \log S_{H\beta} - (4.2 \pm 0.057). \quad (4)$$

In Table 3 we give the new catalog of distances to 843 Galactic PNe, based on Eq. 4. For each PN in the HASH catalog whose $H\beta$ intensity and apparent radius is available we calculate its heliocentric distance, D , based on our scale.

In the catalog we list the PN G name, the angular radius θ , the logarithmic $H\beta$ flux and its uncertainty, the logarithmic extinction constant and its uncertainty, the heliocentric distances

Table 2. Summary of the Distance Scale Analysis

Scale	$\sigma_{\omega_c}/\omega_c$	N_{cal}	Slope	Intercept	ρ_{ab}	N_{comp}	$\langle K \rangle$	$\langle \sigma_K \rangle$
1	<0.05	26	-0.232 ± 0.010	-4.075 ± 0.132	0.99	26 (1) 355 (2)	0.894 0.913	0.102 0.544
2	<0.10	74	-0.237 ± 0.005	-4.14 ± 0.070	0.99	74 (1) 355 (2)	0.914 0.917	0.113 0.543
3	<0.20	137	-0.242 ± 0.004	-4.20 ± 0.057	0.99	133 (1) 355 (2)	0.964 0.931	0.154 0.553

Notes. N_{cal} =number of calibrators; N_{comp} = number of PNe used to compute $\langle K \rangle$ and $\langle \sigma_K \rangle$:

in group (1) we used the Calibrator Sample with the additional requirement of $\log M_i > -2$, and in group (2) we included all PNe with a distance and a parallax determination, and again $\log M_i > -2$.

Table 3. Catalog of Statistical Distances and Peculiar Velocities of Galactic PNe

PN G	θ [$''$]	$F_{\text{H}\beta}$ [$\text{erg cm}^{-2} \text{s}^{-1}$]	c	D [kpc]	V_{pec} [km s^{-1}]	Pop.
000.1+17.2	1.12	-11.91 ± 0.00	0.70 ± 0.10	$8.341^{+0.689}_{-0.636}$	160.21 ± 28.83	Bulge
000.2-01.9	4.47	-12.56 ± 0.01	2.04 ± 0.10	$2.793^{+0.229}_{-0.211}$	50.95 ± 12.12	Disk
000.3+12.2	5.82	-10.88 ± 0.01	0.55 ± 0.06	$2.188^{+0.137}_{-0.048}$	48.23 ± 9.72	Disk

Notes. Distances are obtained from Scale number 3 of Table 2; see main text for a detailed column description.

(The full table is available electronically at the CDS.)

from our scale of Eq. 4, D [kpc], and their left/right formal uncertainties. The latter have been computed by estimating $\sigma_{\log D}$ via first-order error propagation of the linear relations among the variables $\log R$, $\log S_{\text{H}\beta}$, θ and D , accounting for uncertainties in both observed and fitted parameters; then, asymmetric uncertainties were defined by putting $\sigma_{D^-} = 10^{(\log D - \sigma_{\log D})}$ and $\sigma_{D^+} = 10^{(\log D + \sigma_{\log D})}$. Finally, we include the PN peculiar velocity V_{pec} and its uncertainty calculated from Eq. 12, plus a Disk/Bulge/Halo population classification as discussed in the following section.

3. Planetary Nebulae as tracers of the Galactic Disk

An important scientific motivation for the Galactic PN distance scale is the study of the radial (and vertical) metallicity gradients in the Galaxy.

Planetary nebulae are the ejecta of evolved 1-8 M_{\odot} stars, thus they represent a continuum of stellar populations from very old ages through relatively young, with ages ~ 0 to ~ 10 Gyr, which makes them very versatile probes for Galactic evolution. Gas-phase abundances of α -elements observed through emission-lines and measured in their shell should be the same as their progenitors' at the time of formation, since these elements do not change considerably during the evolution of these stars. Thus, tracing the abundances of such elements is equivalent to probing the Galaxy's abundance with look-back time from ~ 0 to ~ 10 Gyr, depending on the initial progenitor mass of the PNe.

3.1. Elemental abundances

We use PN elemental abundances both for progenitor dating purposes, and to determine the metallicity gradients. We select the elemental abundances from all references included in Stanghellini & Haywood (2018), to whose we add the abundances from the data sets by Tsamis et al. (2003), Miller et al. (2019), McNabb et al. (2016), and Delgado-Inglada et al. (2015),

which were not included therein. In the references where abundances are given both for the whole nebula and for different parts of the PN, we use only those measures based on spectra that include the whole PN, so abundances from different references are readily comparable with one another. The final abundances have been curated, i.e., we have recalculated the ionization correction factor (ICF) uniformly, as described in Stanghellini & Haywood (2018).

In Table 4 we give the average abundances used in this paper. Column (1) gives the PN G name, then in columns (2) through (4) we give the C, N, and O abundances, in the usual scale $\log(X/H)+12$, averaged from all the available references. The uncertainties, given in dex, are the dispersion of that elemental abundance across the literature, estimated with $\sigma(\log(O/H)) = 0.434 \times [\sigma(O/H)/\langle O/H \rangle]$. We also produced a curated catalog of selected PN abundances, shown in Table 5. For this selection we prioritize abundances from space-based observations unless they are deemed uncertain in the original papers; otherwise, we use the published ground-based abundances, prioritizing the most recent, or recently revised, ones. Curated abundances are given with their uncertainty, when available in the original reference.

3.2. Velocities of PNe Central Stars

For a sizable sample of CSs whose PNe have a statistical distance in our catalog, Gaia DR3 provides equatorial proper motions $\mu_{\alpha^*} \pm \sigma_{\mu_{\alpha^*}}$, $\mu_{\delta} \pm \sigma_{\mu_{\delta}}$; we use this kinematic information as insight for their populations and ages. After converting DR3 proper motions and their standard deviations in galactic coordinates $\mu_l \pm \sigma_{\mu_l}$, $\mu_b \pm \sigma_{\mu_b}$ via the transformation matrices A'_G and C_{Gal} defined by Eq. 4.62 and 4.79 of the Gaia EDR3 online

² the asterisk, indicating that the longitudinal proper motion is measured along the great circle at the star's location, will be dropped and implicitly assumed in the following.

Table 4. Averaged Elemental Abundances of Galactic PNe

PN G	log(C/H)+12	log(N/H)+12	log(O/H)+12	Prog. Age
002.7-04.8	9.02±0.20	8.68±0.27	8.68±0.20	OPPN
006.1+08.3	8.58±0.20	7.92±0.17	8.57±0.20	OPPN
010.1+00.7	8.23±0.20	8.65±0.20	8.26±0.20	YPPN

Notes. Elemental abundances have been averaged from all references included in Stanghellini & Haywood (2018), Tsamis et al. (2003), Miller et al. (2019), McNabb et al. (2016), and Delgado-Inglada et al. (2015); the age of the PPN progenitor (OPPN=old, YPPN=young) is defined according to Stanghellini & Haywood (2018) and Ventura et al. (2016), see text.

(The full table is available electronically at the CDS.)

Table 5. Selected Elemental Abundances of Galactic PNe

PN G	log(C/H)+12	log(N/H)+12	log(O/H)+12	Prog. Age
002.7-04.8	9.02±0.20	8.68±0.20	8.48±0.20	OPPN
006.1+08.3	8.58±0.20	8.03±0.20	8.58±0.20	OPPN
010.1+00.7	8.23±0.20	8.65±0.20	8.26±0.20	YPPN

Notes. In the computation of abundances, space-based observations and most recent ground-based abundances have been prioritized (see main text)

(The full table is available electronically at the CDS.)

documentation, we compute the corresponding observed spatial velocities plus errors, given in [km s⁻¹], as

$$V_l = 4.740470446 \mu_l \times D \quad (5)$$

$$\sigma_{V_l} = 4.7407470446 \times D \sqrt{\mu_l^2 \sigma_D^2 + \sigma_{\mu_l}^2}$$

$$V_b = 4.74047 \mu_b \times D \quad (6)$$

$$\sigma_{V_b} = 4.74074 \times D \sqrt{\mu_b^2 \sigma_D^2 + \sigma_{\mu_b}^2}$$

where l and b are the Galactic longitude and latitude. We also adopt $\sigma_D \equiv (\sigma_{\text{rad}} + \sigma_{\text{D}^+})/2$. The third component of the velocity is the radial component, V_r , which has been observed independently for 498 PNe of our sample (Durand et al. 1998)³.

Having secured distances and kinematic data for these stars, we can estimate their *peculiar* velocity V_{pec} as the residual stellar motion which does not conform to the general Galactic rotation. To this end, we assumed an empirical model for the Galactic rotation curve which follows Eilers et al. (2019) for galactocentric distances larger than 5 kpc, while for inner distances we made use of the results of Bhattacharjee et al. (2014) – who resorted to H I and H II regions, as well as CO emission lines, as tracers of the inner Galactic Disk – adapting their Rotation Curve to the fundamental parameters found by Eilers et al. (2019), i.e., $R_\odot = 8.122$ kpc, the galactocentric distance of the Sun, and $V_{\text{LSR}} = 229$ [km s⁻¹], the circular velocity of the Local Standard of Rest (LSR). We have combined these data into a grid of Galactic radii and corresponding rotation velocities, plus uncertainties, given in Table 6. Moreover, in the following calculations, the velocity of the Sun with respect to the LSR has been set to $(U_\odot, V_\odot, W_\odot) = (11.1, 12.4, 7.25)$ [km s⁻¹], according to Schönrich et al. (2010).

We first transform the observed spatial velocities into cartesian components along the *local triad* at the star as

$$\mathbf{v}_{\text{rel}} = (\mathbf{e}_l \quad \mathbf{e}_b \quad \mathbf{e}_r) \cdot \begin{pmatrix} V_l \\ V_b \\ V_r \end{pmatrix} \equiv A \cdot \begin{pmatrix} V_l \\ V_b \\ V_r \end{pmatrix} \quad (7)$$

³ Gaia DR3 had measured radial velocities for only 13 CSs of our Calibrator Sample

Table 6. Adopted Galactic Rotation Curve¹

R_G [kpc]	V_c [km/s]	R_G [kpc]	V_c [km/s]
1.62	208.42 ^{+5.80} _{-5.80}	13.74	217.47 ^{+0.64} _{-0.51}
2.61	206.23 ^{+1.60} _{-1.60}	14.24	217.31 ^{+0.77} _{-0.66}
3.55	218.98 ^{+2.54} _{-2.54}	14.74	217.60 ^{+0.65} _{-0.68}
4.52	238.93 ^{+2.20} _{-2.20}	15.22	217.07 ^{+1.06} _{-0.80}
5.27	226.83 ^{+1.91} _{-1.90}	15.74	217.38 ^{+0.84} _{-1.07}
5.74	230.80 ^{+1.43} _{-1.34}	16.24	216.14 ^{+1.20} _{-1.48}
6.23	231.20 ^{+1.70} _{-1.10}	16.74	212.52 ^{+1.39} _{-1.43}
6.73	229.88 ^{+1.44} _{-1.32}	17.25	216.41 ^{+1.44} _{-1.85}
7.22	229.61 ^{+1.37} _{-1.11}	17.75	213.70 ^{+2.22} _{-1.65}
7.82	229.91 ^{+0.92} _{-0.88}	18.24	207.89 ^{+1.76} _{-1.88}
8.19	228.86 ^{+0.80} _{-0.67}	18.74	209.60 ^{+2.31} _{-2.77}
8.78	226.50 ^{+1.07} _{-0.95}	19.22	206.45 ^{+2.54} _{-2.36}
9.27	226.20 ^{+0.72} _{-0.62}	19.71	201.91 ^{+2.99} _{-2.26}
9.76	225.94 ^{+0.42} _{-0.52}	20.27	199.84 ^{+3.15} _{-2.89}
10.26	225.68 ^{+0.44} _{-0.40}	20.78	198.14 ^{+3.33} _{-3.37}
10.75	224.73 ^{+0.38} _{-0.41}	21.24	195.30 ^{+3.99} _{-6.50}
11.25	224.02 ^{+0.33} _{-0.54}	21.80	213.67 ^{+15.38} _{-18.18}
11.75	223.86 ^{+0.40} _{-0.39}	22.14	176.97 ^{+28.38} _{-18.37}
12.25	222.23 ^{+0.51} _{-0.37}	22.73	193.11 ^{+27.64} _{-19.05}
12.74	220.77 ^{+0.54} _{-0.46}	23.66	176.63 ^{+18.67} _{-16.74}
13.23	220.92 ^{+0.57} _{-0.40}	24.82	198.42 ^{+6.50} _{-6.12}

Notes. ⁽¹⁾ Derived from Eilers et al. (2019) and Bhattacharjee et al. (2014)

where

$\mathbf{e}_l^T = (-\sin l, \cos l, 0)$, $\mathbf{e}_b^T = (-\sin b \cos l, -\sin b \sin l, \cos b)$, $\mathbf{e}_r^T = (\cos b \cos l, \cos b \sin l, \sin b)$, and A is the so-called direction cosine matrix representing the rotation to the local frame.

To derive galactocentric velocities we must account for the Sun's galactocentric velocity, i.e. $\mathbf{v}_\odot = (U_\odot, V_\odot + V_{\text{LSR}}, W_\odot)$, so

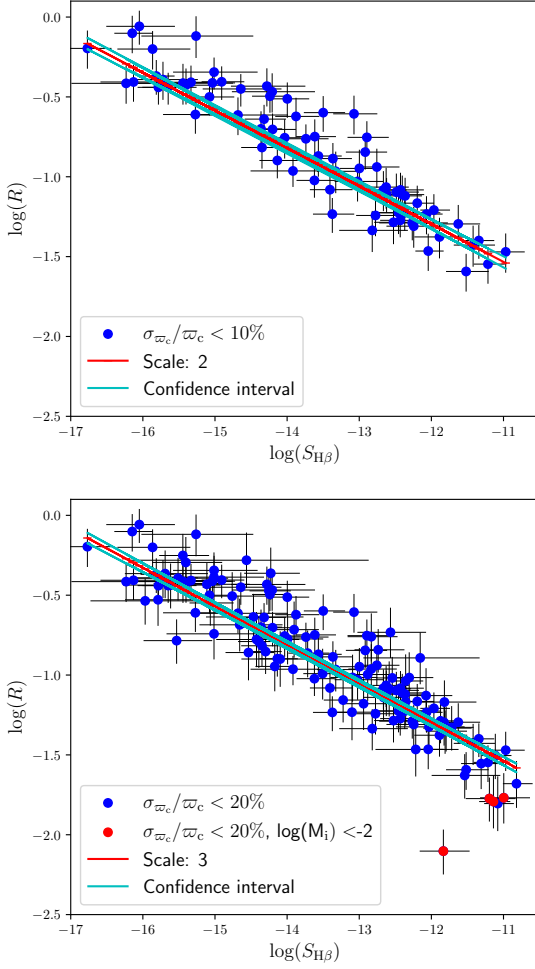


Fig. 1. The $\log(R)$ [pc] vs. $\log(S_{H\beta})$ [$\text{erg cm}^{-2} \text{s}^{-1}$] plot for calibrators with $\sigma_{\omega_c}/\omega_c < 0.1$ (top panel) and $\sigma_{\omega_c}/\omega_c < 0.2$ (bottom panel). In both plots, the blue points are the calibrators, with their logarithmic (asymmetric) error bars reflecting the 1- σ uncertainties of the observed parameters; In the bottom plot the red points are those calibrators with $\log M_i < -2$; the red line are the two distance scales from the calibrators, and in cyan we plot the 2- σ confidence band of the scales, representing the uncertainty of the logarithmic radius R induced by the correlated errors on \hat{a} and \hat{b}

that

$$\mathbf{v}_{gal} = \begin{pmatrix} U \\ V \\ W \end{pmatrix} = \mathbf{v}_{rel} + \mathbf{v}_{\odot} \quad (8)$$

For the following analysis, it is useful to express spatial velocities in cylindrical coordinates, for which we need to compute the galactocentric azimuth ϕ as (e.g. López-Corredoira & Sylos Labini 2019)

$$\begin{aligned} X &= R_{\odot} - D \cos l \cos b \\ Y &= D \sin l \cos b \\ \phi &= \tan^{-1} Y/X \end{aligned}$$

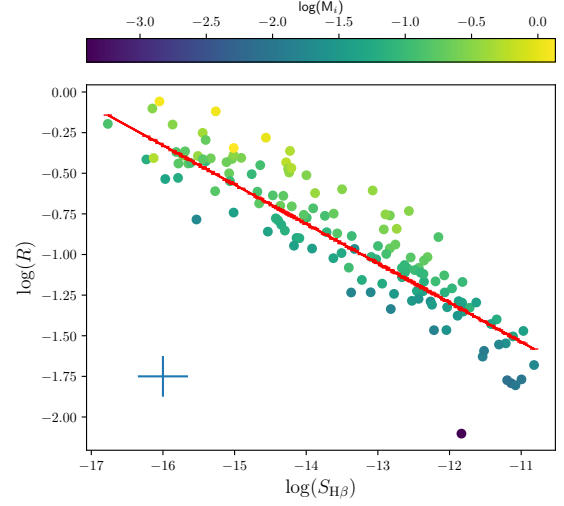


Fig. 2. The $\log(R)$ [pc] vs. $\log(S_{H\beta})$ [$\text{erg cm}^{-2} \text{s}^{-1}$] plot for the PN sample with $\sigma_{\omega_c}/\omega_c < 0.2$, colour-coded according to their ionized mass. The error bars have been omitted for clarity; the cross at the bottom-left corner is representative of the typical error in the respective axis

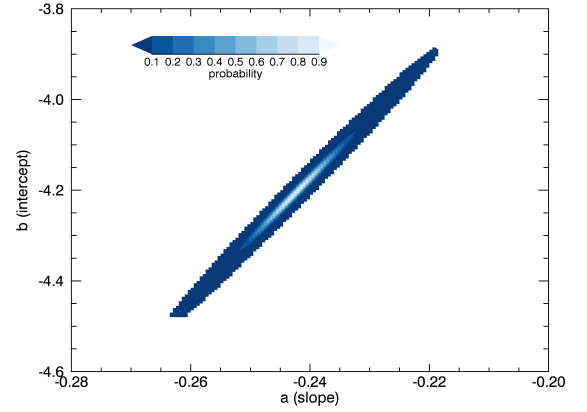


Fig. 3. Normalized 2D posterior probability of the distance scale parameters obtained from the PN sample with $\sigma_{\omega_c}/\omega_c < 0.20\%$

where D is the star's heliocentric distance and ϕ is taken as positive in the direction of galactic rotation; the radial, azimuthal, and vertical components of the spatial velocity are then given by:

$$\begin{aligned} V_R &= -U \cos \phi + V \sin \phi \\ V_{\phi} &= U \sin \phi + V \cos \phi \\ V_z &= W \end{aligned} \quad (10)$$

Finally, we are able to estimate the peculiar velocity of each star by subtracting from the azimuthal component V_{ϕ} the circular motion due to differential galactic rotation. To do so, for each PN we compute the galactocentric radius R_G projected onto the Galactic plane as:

$$R_G = \sqrt{R_{\odot}^2 + D^2 \cos^2 b - 2R_{\odot}D \cos l \cos b}, \quad (11)$$

and interpolate linearly between the nearest two values of R_G of Table 6 to calculate the star's circular velocity $V_c(R_G)$.

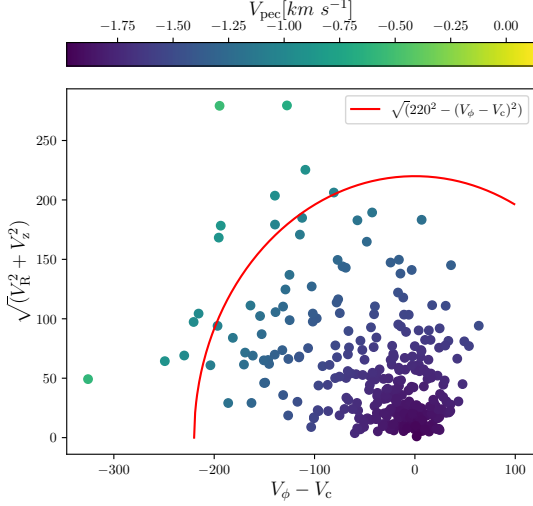


Fig. 4. Halo PNe selected through the velocity analysis of the CSs, by means of the Toomre diagram. The colour bar is coded for the peculiar velocities as in Eq. 12. The dots outside the region encircled by the red curve correspond to Halo PNe.

The absolute space motion of the stars (or the PNe), which we call V_{pec} , can be obtained by quadrature of the three velocity components as

$$V_{\text{pec}} = \sqrt{V_R^2 + V_z^2 + (V_\phi - V_c)^2} \quad (12)$$

$$\sigma_{V_{\text{pec}}} \approx \sqrt{\sigma_{V_1}^2 + \sigma_{V_b}^2 + \sigma_{V_r}^2}$$

where $\sigma_{V_{\text{pec}}}$ is a lower-limit uncertainty, which assumes uncorrelated variables and perfect model. Peculiar velocities for the PNe are reported in Table 3.

In Figure 4 we put the inferred peculiar velocities in the so-called Toomre diagram, which can be used to identify regions of high probability of finding Disk versus Halo stars. In particular, following Bonaca et al. (2017), we use $V_{\text{pec}} > 220$ [km s⁻¹] as threshold value for rejecting Halo stars.

3.3. Galactic PN Populations, and Dating PN progenitors

We derive heliocentric distances D and their confidence limits, as described in subsection 2.3, for 843 Galactic PNe. The range of distances spanned by these PNe is ~ 150 to $\sim 27,000$ [pc], and most of them can be included in a general Disk population, thus they are adequate for our science scope. We populate the Halo PN sample selecting them by peculiar velocity, where Halo PNe have $V_{\text{pec}} > 220$ [km s⁻¹]. This selection yields to 13 Halo PNe. We also tentatively define the Bulge population similarly to Stanghellini & Haywood (2018), by selecting those PNe in the central 3×3 [kpc], thus with $|z| < 3$ and $0 < R_G < 3$ [kpc]. To constrain the Bulge sample even more we select in this sample only those PNe whose apparent radius is $\theta < 5$ [arcsec]. Our selection gives 102 Bulge PNe. Whether a PN belongs to the Halo or Bulge populations, according to our selection, is noted in Table 3.

In Figure 5 we plot the distribution of the peculiar velocity vs. z , where the colour indicates the distance from the Galactic center. We observe that in the area between the two grey lines

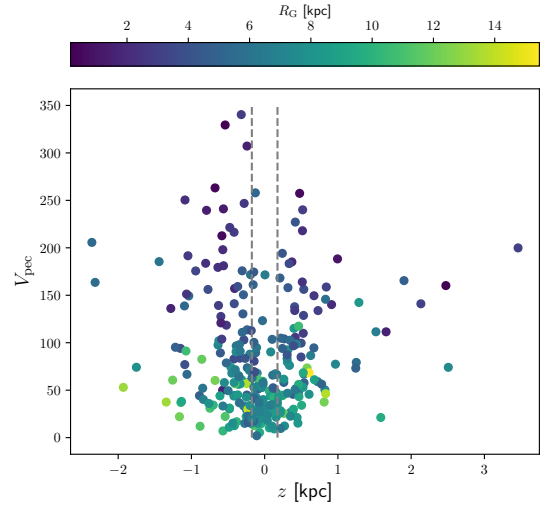


Fig. 5. Galactic distribution of V_{pec} from Eq. 12, with Galactic altitude, where the colour is coded for the distance from the Galactic center R_G . The vertical thin lines encompass $|z| < 0.175$ zone.

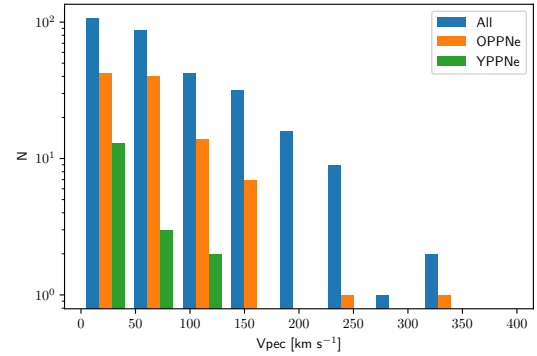


Fig. 6. Histogram of the spatial peculiar velocity V_{pec} [km s⁻¹] for the general Disk population, and for the OPPNe and YPPNe separately. The velocity bin is 10 km s⁻¹. The y-axis is in logarithmic scale.

(± 0.175 kpc) PNe with high peculiar velocity are away from the Galactic center. It is worth noting that all Bulge PNe selected as in §3.3 are outside the grey lines, and have intermediate V_{pec} .

Dating PN progenitors is not trivial, and it has been attempted by Peimbert and Torres-Peimbert, by dividing Galactic PNe into populations (i.e., PN Types I through V). This approach utilizes both the chemistry of the PNe and their kinematics. Stanghellini & Haywood (2018) used the final yields of the *evolutionary* elements, compared to nebular abundances of carbon and nitrogen to select two PN's progenitor populations with extreme ages, called OPPNe (old progenitors PNe, with progenitor ages > 7.5 Gyr), and YPPNe (young progenitors PNe, with progenitor ages < 1 Gyr). This selection is based on the observation that PNe with old and young progenitors occupy markedly different loci on the N/H versus C/H, and N/H vs. O/H, planes. Fig. 2 of Ventura et al. (2016) was used to determine that OPPNe have $C/H > N/H$ or $[\log(N/H) + 12] < 0.8 \times [\log(O/H) + 12] + 1.4$, and YPPNe have $C/H < N/H$ or $[\log(N/H) + 12] > 0.6 \times [\log(O/H) + 12] + 3.3$. In Tables 4 and 5, column 5, we give the PN progenitor age group as derived above, when available.

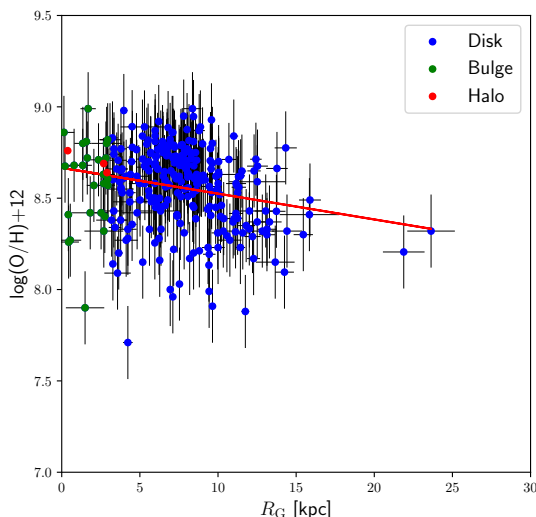


Fig. 7. Radial oxygen gradients for the complete PN sample for which we have a statistical distance and at least one O/H measurement in the literature. Oxygen abundances are averages of all published abundances, and the error bars represent the dispersion. All PNe have been included in these plots, and Halo and Bulge populations are indicated with different colours. The red line is the linear fit to the data; slopes and intercepts for the different populations are in Table 7.

More insight on dating PN progenitors are derived from the comparison of Gaia proper motions described in the previous sub-section, with the ages derived purely from the PN chemistry above. In Figure 6 we show the resulting distribution of V_{pec} for the general PN population (which includes OPPNe, YPPNe, as well as the intermediate age progenitor PNe, and those PNe whose age from chemistry was unavailable), then by plotting separately OPPNe and YPPNe. We find that the OPPNe distribution peaks at $V_{\text{pec}} \sim 60$ [km s $^{-1}$], while the YPPNe distribution peaks at a smaller velocity ($\sim 25 - 30$ [km s $^{-1}$]). This plot shows the correlation between completely independent dating systems, from the chemistry and the kinematics of the PNe, giving us confidence about using the OPPNe and YPPNe distributions.

3.4. Galactic metallicity gradients and other metallicity variations

The radial metallicity gradients in this paper have been calculated by orthogonal distance regression, which makes use of the uncertainties in the measured quantities R_G and $\log(\text{O}/\text{H}) + 12$. The uncertainties in the elemental abundances are described in §3.1, where we indicate which literature fonts we chose the abundances from, and how errors are estimated both in the average and chosen abundances (see Table 4). The uncertainties in R_G are computed by first-order propagation of the symmetrized error of the distance scale, $\sigma_D = (\sigma_{D^-} + \sigma_{D^+})/2$, thus obtaining $\sigma_{R_G} = |D \cos^2 b - R_G \cos l \cos b| \cdot \sigma_D / R_G$. The regression yields to a slope and an intercept, along with their formal errors.

In Table 7 we present the estimation of the gradient slopes obtained using different subsets of PNe, and with both averaged and selected chemical abundances. We utilize all PNe where at least one oxygen measurement was available in the literature, excluding only the extreme outliers ($\log(\text{O}/\text{H}) + 12 < 7.5$ and $\log(\text{O}/\text{H}) + 12 > 9$). All radial oxygen gradients that we derive

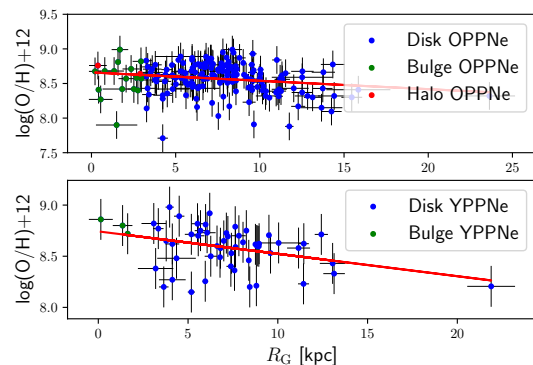


Fig. 8. Radial oxygen gradients for the OPPN (top) and the YPPN (bottom) populations. All PNe have been included in these plots, and Halo and Bulge populations are indicated with different colours. Oxygen abundances are the selected ones here. The red lines are the linear fits of the data; slopes and intercepts for the different populations are in Table 7.

in this paper have negative slopes. The general PN population (Fig. 7 has gradient slope of -0.0144 ± 0.00385 [dex kpc $^{-1}$] when we use the average abundances. By excluding the Halo population (2 PNe??) the gradient does not change significantly.

For all comparable samples, the evolution goes in the direction of gradients steepening with time since Galaxy formation. In fact, for the OPPN and YPPN populations we derive gradient slopes $\Delta \log(\text{O}/\text{H}) / \Delta R_G = -0.0121 \pm 0.00465$ and -0.022 ± 0.00758 [dex kpc $^{-1}$] respectively when we use average abundances, and $\Delta \log(\text{O}/\text{H}) / \Delta R_G = -0.0132 \pm 0.00464$ and -0.0278 ± 0.00789 [dex kpc $^{-1}$] respectively if we use the selected abundances (plots in Fig. 8). This result indicates a mild – but significant when compared to the uncertainties – evolution of the metallicity gradient with time. Our results point to a steeper gradient slope for the younger stellar population than for the older stellar population, with slope difference of ~ 0.15 dex. This implies a slow time evolution of the gradient. The time evolution of the gradient slope does not vary whether or not we include Halo PNe in the OPPN sample (see Table 7).

It is beyond the scope of this paper to discuss the causes for gradient steepening. Chemical evolutionary models of star forming galaxies (Gibson et al. 2013) indicate that steepening with time of the radial metallicity gradients occurs when the chemical evolution proceeds with feedback of fresh, metal poor gas from the environment. Such models can not predict the gradient ab initio, thus, metallicity gradients for old populations such as those from OPPNe represent a precious constraint.

Finally, we tested the oxygen evolution (or chemical enrichment) by comparing average oxygen abundances in the OPPNe and YPPNe samples, to derive an average Galactic enrichment of ~ 0.06 dex between the age > 7.5 Gyr and the age < 1 Gyr populations.

4. Results and conclusions

This paper yields essentially to three novel results for PNe in the Galactic environment. First, we produced a new distance scale based on DR3 parallaxes, which is given in Eq.4. Distances derived from the new scale are published as a catalog in this paper (Table 3). By comparing our new distances with the DR3 CS parallaxes, as in the analysis by Smith (2015), we find $\langle K \rangle = 0.964$, where $K = D \times \varpi_c$, and $\langle \sigma_K \rangle = 0.154$ if

Table 7. Radial Oxygen Gradients

Sample	N	slope [dex kpc ⁻¹]	intercept log(O/H)+12
Average abundances			
All	288	-0.0144±0.00385	8.669±0.0307
Excluding Halo PNe	285	-0.0141±0.00390	8.666±0.0314
OPPNe	186	-0.0121±0.00465	8.660±0.0376
YPPNe	55	-0.0220±0.00758	8.743±0.0601
Selected abundances			
All	288	-0.0163±0.00385	8.672±0.0312
Excluding Halo PNe	285	-0.0159±0.00392	8.668±0.0319
OPPNe	186	-0.0132±0.00464	8.659±0.0373
YPPNe	55	-0.0278±0.00789	8.759±0.0629

Notes. Gradients are estimated using chemical abundances from Tables 4 (Average abundances) and 5 (Selected abundances), and for the listed PN samples, of numerosity N.

we exclude from the comparison the PNe with $\log M_i < -2$, and $< K > = 0.931$ if we include all calibrators. Comparing these results with those of Paper I, where the best scale obtained with DR2 parallaxes gave $< K > = 0.948$ and $< \sigma_K > = 0.25$, we conclude that the use of DR3 parallaxes as calibrators successfully improved upon the Galactic PN distance scale.

We have calculated $< K >$ based on DR3 parallaxes for the most commonly used PN distance scales, such as Frew et al. (2016) (hereafter FPB) and Stanghellini et al. (2008) (hereafter SSV). We found $< K_{FPB} > = < D_{FPB} \times \varpi_c > = 1.272$ and $< K_{SSV} > = < D_{SSV} \times \varpi_c > = 1.203$ with the exclusion of calibrators with $\log M_i < -2$, and $< K_{FPB} > = 1.36$ and $< K_{SSV} > = 1.29$ when including all calibrators. We conclude that the scale presented in Eq.4 gives the most reliable distances to date, and distances in Table 3 should be used, unless an accurate parallax measurement of the CS or PN under study is available, from DR3 or otherwise. Moreover, our analysis revealed that the $\log R - \log S_{H\beta}$ distance scale of Galactic PNe has an intrinsic mean dispersion of ≈ 0.1 dex around the $\log R - \log S_{H\beta}$ linear relation, which can be accounted for by the variation of the PN ionized mass (excluding objects with $\log M_i < -2$), bringing us to the conclusion that statistical distance scales such as this can hardly be improved by increasing the accuracy of calibrators.

Second, we used Gaia DR3 proper motion to have a thorough description of the peculiar velocities of the CSs, or the PNe, and to characterize the Halo population. The peculiar velocity derivation has the additional advantage to be a completely independent assessment of the progenitor ages of the PNe, thus validating even further the OPPN and YPPN classes based on elemental abundances ratios C/O and N/O. The proper motion and peculiar velocity analysis of § 3.2 provided a tool to exclude Halo PNe from the gradient analysis. Even more importantly, it gave us additional confidence in the progenitor dating from chemical analysis, as described in § 3.3. This is, to our knowledge, the first time that dating PNe is consistent with two completely independent approaches, while in the past the dating scheme has used either approach, or both approaches for different age classes, such as in defining Peimbert's PN Types (Peimbert 1978). Dating PN progenitors is essential to study the time evolution of the radial metallicity gradients in the Milky Way.

Third, we measure radial oxygen gradients based on DR3 distance scale, with Halo PN selected through their kinematic properties measured by Gaia DR3, and progenitor ages from chemical evolutionary assessment, confirmed via the peculiar velocities determined by Gaia. The negative, shallow gradients

that we determine, and the mild evolution of the gradients – steepening since the formation of the Galaxy – are a confirmation of past results both in the Galaxy (Stanghellini & Haywood 2018) and in the nearby spiral galaxies examined (Peña & Flores-Durán 2019; Magrini et al. 2016), where all emission-line probes in star-forming galaxies (including the Milky Way) indicate that the oxygen radial gradients are steeper in the younger populations. For the gradients we have used curated catalogs of published abundances, which we give in Tables 4 and 5.

It is worth noting that, while our results confirm most of the metallicity gradients measurements based on gas-phase data published to date, recent cluster and stellar results show a more controversial picture (Anders et al. 2017; Magrini et al. 2023; Gaia Collaboration et al. 2023a). Stellar metallicity are mainly inferred from iron rather than oxygen; since iron atoms in PNe are mostly found in condensed state (e.g. Delgado-Inglada et al. 2015), a direct comparison between the stellar and nebular samples is typically problematic.

The work of Magrini et al. (2023) also include α -element gradients, indicating minimal oxygen gradient evolution, compatible with flattening of gradients with time. Their oxygen gradient slopes of the age<1 Gyr and age>3 Gyr bins in their table A.10. are the same within the uncertainties. We underline that these results are not incompatible with ours, since we are comparing different age ranges: our PN progenitors are in the age<1 Gyr and age>7.5 Gyr bins, whereas their oldest clusters are within 7 Gyr. Furthermore, migration, and evolution due to inflow, of clusters and stars may be different in ways that are unpredictable when measuring radial gradients.

Interestingly, (Bhattacharya et al. 2022) who studied the radial oxygen gradients in M31, found that young, thin disk PNe describe a steeper radial gradient than the older, thick disk population, in qualitative agreement with our results, where radial metallicity gradients steepen with galaxy evolution. Quantitatively, in their Fig. 13 they attempt to unify the gradients slopes across galaxies, taking into account their scale lengths, and show the remarkable similarities between oxygen gradients in the Galaxy and M31.

More inspection of Galactic gradients from data and modeling comes from the recent analysis in Lian et al. (2023), where they use integrated radial metallicities to find (see their Fig. 1) that radial Fe/H gradients from older populations are flatter than for the young population, in agreement with our results. They also compared the Galactic gradient from present-day stellar population with that obtained from gas-phase oxygen (H II re-

gion), which is consistent with the PNe abundance tracers, reinforcing the confidence on our findings.

The distance scale that we presented here, and the distances in our catalog, will be used in the future to study the behaviour of dust and other elements in Galactic PNe in the framework of the chemical evolution of the Galaxy.

Acknowledgements. This work has made use of data from the European Space Agency (ESA) mission *Gaia* (<https://www.cosmos.esa.int/gaia>), processed by the *Gaia* Data Processing and Analysis Consortium (DPAC, <https://www.cosmos.esa.int/web/gaia/dpac/consortium>). Funding for the DPAC has been provided by national institutions, in particular the institutions participating in the *Gaia* Multilateral Agreement. B.B. acknowledges the support of the Italian Space Agency (ASI) through contract 2018-24-HH.0 and its addendum 2018-24-HH.1-2022 to the National Institute for Astrophysics (INAF). The authors would like to thank the anonymous referee whose comments and suggestions helped improving the original manuscript.

References

- Anders, F., Chiappini, C., Minchev, I., et al. 2017, *A&A*, 600, A70
- Bhattacharjee, P., Chaudhury, S., & Kundu, S. 2014, *ApJ*, 785, 63
- Bhattacharya, S., Arnaboldi, M., Caldwell, N., et al. 2022, *MNRAS*, 517, 2343
- Bonaca, A., Conroy, C., Wetzel, A., et al. 2017, *ApJ*, 845, 101
- Chornay, N. & Walton, N. A. 2021, *A&A*, 656
- Curti, M., Maiolino, R., Cirasuolo, M., et al. 2020, *MNRAS*, 492, 821
- Delgado-Inglada, G., Rodríguez, M., Peimbert, M., et al. 2015, *MNRAS*, 449, 1797
- Durand, S., Acker, A., & Zijlstra, A. 1998, *A&AS*, 132, 13
- Eilers, A.-C., Hogg, D. W., Rix, H.-W., et al. 2019, *ApJ*, 871, 120
- Fabrizius, C., Luri, X., Arenou, F., et al. 2021, *A&A*, 649
- Frew, D. J., Parker, Q. A., & Bojčić, I. S. 2016, *MNRAS*, 455, 1459
- Gaia Collaboration, Prusti, T., de Bruijne, J. H. J., et al. 2016, *A&A*, 595, A1
- Gaia Collaboration, Recio-Blanco, A., Kordopatis, G., et al. 2023a, *A&A*, 674, A38
- Gaia Collaboration, Vallenari, A., Brown, A. G. A., et al. 2023b, *A&A*, 674, A1
- Gibson, B. K., Pilkington, K., Brook, C. B., et al. 2013, *A&A*, 554
- González-Santamaría, I., Manteiga, M., Manchado, A., et al. 2021, *A&A*, 656
- Henry, R. B. C., Kwitter, K. B., Jaskot, A. E., et al. 2010, *ApJ*, 724, 748
- Lian, J., Bergemann, M., Pillepich, A., Zasowski, G., & Lane, R. R. 2023, *Nature Astronomy* [arXiv:2306.14100]
- Lindgren, L., Bastian, U., Biermann, M., et al. 2021a, *A&A*, 649, A4
- Lindgren, L., Klioner, S. A., Hernández, J., et al. 2021b, *A&A*, 649, A2
- López-Corredoira, M. & Sylos Labini, F. 2019, *A&A*, 621
- Mackereth, J. T., Bovy, J., Leung, H. W., et al. 2019, *MNRAS*, 489, 176
- Magrini, L., Coccatto, L., Stanghellini, L., et al. 2016, *A&A*, 588
- Magrini, L., Viscasillas Vázquez, C., Spina, L., et al. 2023, *A&A*, 669, A119
- Matteucci, F. 2021, *A&A Rev.*, 29, 5
- McNabb, I. A., Fang, X., & Liu, X.-W. 2016, *MNRAS*, 461, 2818
- Miller, T. R., Henry, R. B. C., Balick, B., et al. 2019, *MNRAS*, 482, 278
- Parker, Q. A., Bojčić, I. S., & Frew, D. J. 2016, *Journal of Physics Conference Series*, 728, 032008
- Peña, M. & Flores-Durán, S. N. 2019, *Rev. Mexicana Astron. Astrofis.*, 55, 255
- Peimbert, M. 1978, in *Planetary Nebulae*, ed. Y. Terzian, Vol. 76, 215–224
- Pottasch, S. R. 1980, *A&A*, 89, 336
- Prantzos, N., Abia, C., Chen, T., et al. 2023, *MNRAS*, 523, 2126
- Schneider, S. E. & Buckley, D. 1996, *ApJ*, 459, 606
- Schönrich, R., Binney, J., & Dehnen, W. 2010, *MNRAS*, 403, 1829
- Shklovsky, I. S. 1956, *AZh*, 33, 222
- Smith, H. 2015, *MNRAS*, 449, 2980
- Stanghellini, L. 2019, *IAU Symposium*, 343, 174
- Stanghellini, L., Berg, D., Bresolin, F., Cunha, K., & Magrini, L. 2019, arXiv e-prints, arXiv:1905.04096
- Stanghellini, L., Bucciarelli, B., Lattanzi, M. G., & Morbidelli, R. 2020, *ApJ*, 889, 21
- Stanghellini, L. & Haywood, M. 2018, *ApJ*, 862, 45
- Stanghellini, L., Shaw, R. A., & Villaver, E. 2008, *ApJ*, 689, 194
- Strömberg, G. 1925, *ApJ*, 61, 363
- Strömberg, G. 1946, *ApJ*, 104, 12
- Tsamis, Y. G., Barlow, M. J., Liu, X. W., Danziger, I. J., & Storey, P. J. 2003, *MNRAS*, 345, 186
- Ventura, P., Stanghellini, L., Di Criscienzo, M., García-Hernández, D. A., & Dell’Agli, F. 2016, *MNRAS*, 460, 3940
- Wielen, R. 1977, *A&A*, 60, 263